ARTICLE IN PRESS

International Journal of Plasticity xxx (2014) xxx–xxx

Contents lists available at ScienceDirect

International Journal of Plasticity

journal homepage: www.elsevier.com/locate/ijplas

Evaluation of biaxial flow stress based on elasto-viscoplastic self-consistent analysis of X-ray diffraction measurements

Youngung Jeong [a,b], Thomas Gnäupel-Herold [c], Frédéric Barlat [a,**], Mark Iadicola [b], Adam Creuziger [b], Myoung-Gyu Lee [d,*]

[a] POSTECH, Graduate Institute of Ferrous Technology, Republic of Korea
[b] NIST, Materials Science and Engineering Division, United States
[c] NIST, Center for Neutron Research, United States
[d] Korea University, Dept. of Materials Science and Engineering, Seoul, Republic of Korea

ARTICLE INFO

Article history:
Received 28 October 2013
Received in final revised form 27 May 2014
Available online xxxx

Keywords:
A. Microstructures
B. Constitutive behaviour
B. Crystal plasticity
B. Elastic-viscoplastic material
X-ray diffraction

ABSTRACT

Biaxial flow behavior of an interstitial free steel sample was investigated with two experimental methods: (1) Marciniak punch test with in situ X-ray diffraction for stress analysis; (2) hydraulic bulge test. The stress analysis based on X-ray diffraction using {2 1 1} lattice planes was accompanied by the use of stress factors and intergranular (IG) strains. Stress factors and IG strains were experimentally obtained *ex situ* on samples after prescribed equi-biaxial deformations. An elasto-viscoplastic self-consistent (EVPSC) crystal plasticity model was used to predict the stress factors and the IG strains. The model predictions of the stress factors were in good agreement with the experiments. However, the predictions of IG strains were in poor agreement with their experimental counterparts. As a result, the flow stress solely based on the computationally predicted stress factors and IG strains was unrealistic. The input of the experimental stress factors and IG strains for stress analysis improved the agreement with a reference flow curve obtained by a hydraulic bulge tester. The resulting flow curves based on X-ray diffraction were in good agreement with that of the bulge test up to an effective strain of 0.3. However, an unrealistic softening was observed in larger deformations regardless of whether the stress factor used were experimentally measured or determined from EVPSC calculations.

1. Introduction

1.1. Importance of biaxial flow behavior

Constitutive models, which link imposed strains to resulting stresses, are often populated with experimental flow behavior in uniaxial tension. Uniaxial tension tests are relatively easy to conduct compared to multiaxial experiments such as tests conducted in Mohr and Jacquemin (2008) and Mohr and Oswald (2008), yet, provide useful information (Hill, 1948, 1979; Logan and Hosford, 1980). However, relying solely on uniaxial tension data may lead to erroneous descriptions of biaxial states for anisotropic materials and may prove to be inaccurate. In such cases, the experimental measurement of biaxial properties for comparison with the constitutive model predictions (Kuwabara, 2007; Kuwabara et al., 1998; Xu and

* Corresponding author. Tel.: +82 02 3290 3261; fax: +82 02 928 3584.
** Co-corresponding author.
E-mail addresses: youngung.jeong@nist.gov (Y. Jeong), thomas.gnaeupel-herold@nist.gov (T. Gnäupel-Herold), f.barlat@postech.ac.kr (F. Barlat), mark.iadicola@nist.gov (M. Iadicola), adam.creuziger@nist.gov (A. Creuziger), myounggyu.lee@gmail.com (M.-G. Lee).

http://dx.doi.org/10.1016/j.ijplas.2014.06.009
0749-6419/

Barlat, 2008) may be required. In parallel with experimental progress, some advanced constitutive models have been developed. These advanced models allow the direct input of the in-plane biaxial yield stress in addition to that of uniaxial tension, enhancing the accuracy of finite element (FE) predictions (Barlat et al., 2005, 2003, 1997).

The biaxial behavior is also important for the assessment of sheet metal formability, conventionally characterized by the forming limit curve (FLC). A strain-based FLC is usually represented in the space of the two in-plane principal strains (Marciniak et al., 1973). A stress-based FLC has been proposed to deal with path dependency of the FLC, as the path dependency in strain space is remarkably reduced in stress space (Stoughton, 2000; Stoughton and Zhu, 2004; Wu et al., 2005). However, verification of a path-independent stress-based forming limit approach often relies on constitutive models where stresses are inferred from measured plastic strains.

1.2. Difficulties in biaxial stress measurement

The analysis of biaxial experiments to extract constitutive relationships is not a trivial task. There have been various experimental methods reported in the literature: bulge (Hill, 1950), Nakajima (Lee et al., 2004), Marciniak (Marciniak et al., 1973), tubular (Kuwabara et al., 2005), cruciform (Kuwabara et al., 1998; Verma et al., 2010) and disk compression (Xu and Barlat, 2008) tests. However, some of the listed test methods are only suitable for specific and limited information such as biaxial plastic flow anisotropy (disk compression) or maximum achievable biaxial strain (Nakajima and Marciniak tests). In tests where a punch applies deformation to the surface, the measurement of the stress in the sample is convoluted with friction tractions between the punch and the specimen surface. In tests based on cruciform samples, the achievable deformation is limited by premature fracture caused by the sample geometry. However, an extended deformation in this case is achievable, for instance, by thinning the gauge area (Lebedev and Muzyka, 1998). Samples subjected to either bulge or tubular hydraulic tests can experience an extended amount of deformation without the disturbance caused by friction. However, the deformation conducted in bulge systems contains a component of bending. A more detailed review of various biaxial testing methods is available in a recent article by Tasan et al. (2012). The Marciniak test has advantages such as the in-plane and frictionless conditions in a central area of the specimen (Bong et al., 2012). However, the unquantified friction tractions make measurement of the stress in the sheet from the punch force difficult to deconvolute.

1.3. Stress analysis based on diffraction measurement

Foecke et al. (2007) overcame the difficulties in stress measurement for Marciniak test by employing an in situ X-ray system to measure the stress. In their work, the stress–strain curves of an aluminum alloy were successfully measured based on the in situ lattice strain with known diffraction elastic constants. Later Iadicola et al. (2008) measured multiaxial stress states that included plane strain states to compare the results with predictions made by various yield functions. It is worth mentioning that both studies were conducted for aluminum alloys. Despite of these two successful examples, some issues need to be overcome in order to make diffraction stress analysis more practical for general applications.

For instance, it is well known that the commonly used $\sin^2\psi$ method, which was used in the mentioned work, is not suitable for many steel sheet products due to: (1) the elastic anisotropy, (2) crystallographic texture, and (3) nonspherical grain morphology (Daymond et al., 2000; Lebensohn et al., 1998; Wong and Dawson, 2010), which evolves as further deformation is applied. Steel alloys exhibit higher anisotropic elastic constants compared to the aluminum alloys mentioned earlier, which lead to more complex behavior in the plastic region (Clausen et al., 1998). The changes in texture and grain morphology lead to a strong directional dependence of the elastic constants used to convert lattice strain into macro-stress (Hauk, 1997). Insufficient knowledge of the diffraction elastic constants is one of the reasons why diffraction stress measurements in the presence of texture often lead to inaccurate results.

Whenever elastically anisotropic behavior is expected, stress analysis should be accompanied with the use of proper stress factors to obtain accurate data (Hauk, 1997). One should be cautious when considering use of the stress factor method, since stress factors are sensitive to various parameters. In the literature, stress factors have been shown to depend on (1) crystallographic texture and (2) grain morphology (Gnäupel-Herold et al., 2012). In addition, the influence of (3) the selected diffraction plane was demonstrated in a systematic study (Barral et al., 1987). It is also found that intergranular (IG) strain plays an important role for accurate stress analysis based on diffraction (Gnäupel-Herold et al., 2012). In the current paper, the term 'IG strain' exclusively refers to the intergranular strain as the grain volume averaged strain state of a group of grains with two key characteristics: (1) the grains in diffraction are oriented in the same manner and (2) the IG strains are still present in the absence of applied stresses. Variations in lattice strains that occur on even smaller length scales than the grain dimensions are excluded from consideration.

As the preceding discussion shows, the accurate determination of a stress state using a diffraction technique can be an extremely complicated task to properly account for the material states mentioned above. Fortunately, a number of advanced crystal plasticity frameworks, which can account for the mentioned material states, are available (Kanjarla et al., 2012; Lebensohn et al., 1998; Turner and Tomé, 1994; Wang et al., 2010; Wong and Dawson, 2010). Such models may provide a unified tool, by which the accurate analysis of stresses through diffraction can be better understood. Therefore, the goal of the current study is to demonstrate the validity of a chosen polycrystal plasticity model (Wang et al., 2010) in comparison with experimental results. It is expected that a better understanding of the complex nature of the stress analysis based on diffraction can be achieved by comparing model prediction and experimental results in parallel.

Please cite this article in press as: Jeong, Y., et al. Evaluation of biaxial flow stress based on elasto-viscoplastic self-consistent analysis of X-ray diffraction measurements. Int. J. Plasticity (2014), http://dx.doi.org/10.1016/j.ijplas.2014.06.009

1.4. Structure of this article

The multiaxial experiment system consisting of the Marciniak tooling and a portable X-ray goniometer presented in Section 2. Also, experimental conditions for uniaxial tension as well as the bulge test are presented. In Section 3, stress analysis based on the X-ray measurement of lattice spacings is explained in detail. Description of the crystal plasticity model is presented in Section 4. Then, in Section 5, predictions made by the crystal plasticity model are compared with experimental observations. Summary and discussion follow in Section 6.

2. Experiments

2.1. Marciniak in-plane biaxial stretching

The in-plane biaxial stretching of an interstitial free (IF) steel sample of 1.2 mm thickness was conducted using the Marciniak tooling shown in Fig. 1. The sample was stacked to a mild steel washer, in which a circular hole was machined. This circular window eliminates direct contact between the sample, and the rest of the washer reinforces sample against the moving punch. As a result of the upward motion of the ram, the sheet undergoes biaxial expansion. In addition, the unobstructed top surface of the sheet allows strain measurements with digital image correlation (DIC) and the use of X-ray diffraction. Biaxial stretching with various strain ratios can be achieved by adjusting the width of the sample and washer.

In the current study, the IF steel sample was deformed under near equi-biaxial stretching until fracture. The ram displacement and the strain on the sample are not linearly related. Therefore, appropriate ram positions were determined by deforming a sample of the same kind prior to testing.

2.2. X-ray diffraction

A portable low-power X-ray goniometer is placed above the sample. Diffraction scans were performed while the ram was held at a fixed position, applying load to the sample. The orientation of the X-ray diffractometer is described as two rotations from the sample coordinate system, illustrated in Fig. 2. The two coordinate systems (X and $\widehat{X}$) are attached to the sample and the X-ray diffractometer, respectively. The $\widehat{X}_3$ axis is the normal of *hkl* crystal planes in the diffraction condition. The orientation of the crystal planes in diffraction condition is expressed in terms of the two rotation angles, i.e., ϕ (azimuth from rolling direction) and ψ (tilt from the sheet normal). Orientations (ϕ, ψ) used for the in situ d-spacing are confined to discrete rotations: $\phi = -90°$, 0°, 45° and 135°; $\psi = \pm 34.80°$, $\pm 23.60°$, $\pm 19.24°$, $\pm 11.80°$, $\pm 11.20°$, $\pm 4.36°$, and 0.00°. At each ψ angle, a 2° oscillation was imposed to increase the number of grains in the diffraction condition. The X-ray beam path is bisected by the $\widehat{X}_3$ axis with equal angles between the collimator and detector. In the experimental method described, two detectors (left and right) are used each at different ψ angles with separate detectors covering the positive and negative ψ ranges, respectively. The data presented in this paper are limited to the case of $\phi = 0°$ for the sake of clarity. A Cr tube was used, emitting K-α radiation and diffracting on the {2 1 1} lattice planes.

2.3. Bulge test

A bulge test (Ranta-Eskola, 1979) was conducted to provide a complementary experimental biaxial flow curve and a reference curve to fine-tune the slip system hardening parameters for the crystal plasticity model. The diameter of the bulged

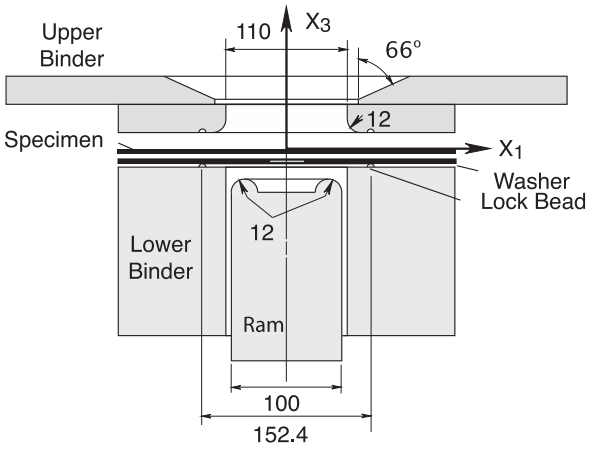

Fig. 1. Cross-section illustration of the axisymmetric Marciniak tooling (Iadicola and Gnäupel-Herold, 2012).

Please cite this article in press as: Jeong, Y., et al. Evaluation of biaxial flow stress based on elasto-viscoplastic self-consistent analysis of X-ray diffraction measurements. Int. J. Plasticity (2014), http://dx.doi.org/10.1016/j.ijplas.2014.06.009

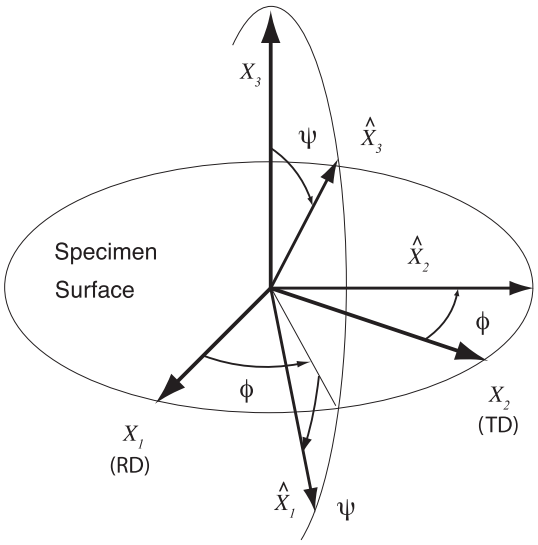

Fig. 2. Coordinate systems used in the diffraction experiments showing the rotation angles ϕ and ψ between sample coordinate system (X) and X-ray coordinate system ($\hat{X}$) (Iadicola and Gnäupel-Herold, 2012).

area was 200 mm. The curvature and strain of the bulged area were determined using a digital image correlation (DIC) system. The sampled areas used for curvature and strain calculation had diameters of 5 mm and 10 mm, respectively. The bulged sample underwent a strain rate on the order of 10^{-3} s^{-1}. The effective flow curves, following (Hill, 1950), were calculated based on several assumptions:

(1) The material is 'incompressible' so that only two principal strain components out of three are independent, by which the thickness strain is calculated from the balanced in-plane principal strain field measured by the DIC system.
(2) The pole of the bulged area is presumed to be perfectly spherical so that the membrane theory can be applied for the calculation of the flow stress based on the hydraulic oil pressure.
(3) The equi-balanced biaxial stress is obtained, as a result of the bulge.

The balanced biaxial stress, $\overline{\Sigma}_b$, is obtained by the above mentioned membrane theory. The stress state of the top bulged sample is then:

$$\overline{\boldsymbol{\Sigma}} = \begin{bmatrix} \overline{\Sigma}_b & 0 & 0 \\ 0 & \overline{\Sigma}_b & 0 \\ 0 & 0 & 0 \end{bmatrix}$$

After adding a hydrostatic stress of '$-\overline{\Sigma}_b$', the above stress tensor becomes equivalent to:

$$\overline{\boldsymbol{\Sigma}} = \begin{bmatrix} 0 & 0 & 0 \\ 0 & 0 & 0 \\ 0 & 0 & -\overline{\Sigma}_b \end{bmatrix}$$

The following plastic strain tensor can be obtained by the incompressibility assumption also by measuring the in-plane biaxial strain $\overline{E}_b$:

$$\overline{\boldsymbol{E}}^p = \begin{bmatrix} \overline{E}_b & 0 & 0 \\ 0 & \overline{E}_b & 0 \\ 0 & 0 & -2\overline{E}_b \end{bmatrix}$$

The contribution of elastic strain is negligibly small at large deformations, thus discarded. Therefore, in case of bulge test, the effective flow curve ($\overline{\Sigma}^{\text{eff}}$ against $\overline{E}^{\text{eff}}$) is constructed by the relationship between $\overline{\Sigma}_b$ and $2\overline{E}_b$.

2.4. Uniaxial tension

Uniaxial tension testing was performed to compare with the experimentally measured biaxial flow curve by the bulge test. The uniaxial tests were conducted at a strain rate in the order of 10^{-3} s^{-1} along the rolling (RD), transverse (TD),

Please cite this article in press as: Jeong, Y., et al. Evaluation of biaxial flow stress based on elasto-viscoplastic self-consistent analysis of X-ray diffraction measurements. Int. J. Plasticity (2014), http://dx.doi.org/10.1016/j.ijplas.2014.06.009

and diagonal (DD) directions. In addition, a relaxation test was conducted to estimate the effect of stress relaxation during the displacement hold required for in situ X-ray measurement. Two extensometers were used to measure longitudinal strain and transverse strain in the gauge area of sample. The ratio between transverse strain $\bar{E}^{w}$ and the thickness strain $\bar{E}^{t}$, i.e. *R*-value, was calculated using the incompressibility condition. The instantaneous *R*-value is defined as:

$$R = \dot{\bar{E}}^{w} \Big/ \dot{\bar{E}}^{t}$$

The stress and plastic strain tensors of the samples under uniaxial tension is as below:

$$\bar{\boldsymbol{\Sigma}} = \begin{bmatrix} \bar{\Sigma}_{l} & 0 & 0 \\ 0 & 0 & 0 \\ 0 & 0 & 0 \end{bmatrix} \quad \text{and} \quad \bar{E} = \begin{bmatrix} \bar{E}_{l} & 0 & 0 \\ 0 & \bar{E}_{w} & 0 \\ 0 & 0 & \bar{E}_{t} \end{bmatrix}$$

The effective stress and strain, in case of uniaxial tension, correspond to $\bar{\Sigma}_{l}$ and $\bar{E}_{l}$, respectively.

3. Stress analysis

When stress is applied to a crystalline material, the lattice *d*-spacing changes elastically (Hauk, 1997; Noyan and Cohen, 1986). The X-ray diffractometer discussed in this paper measures the lattice spacing as a function of orientation (ϕ, ψ) for the given family of diffracting planes $\{hkl\}$. The lattice strain $\varepsilon(hkl, \phi, \psi)$ is obtained from the current *d*-spacing $d(hkl, \phi, \psi)$ and a reference *d*-spacing $d_0(hkl, \phi, \psi)$ at a stress-free state in the following equation:

$$\varepsilon(hkl, \phi, \psi) = \frac{d(hkl, \phi, \psi) - d_0(hkl, \phi, \psi)}{d_0(hkl, \phi, \psi)}. \tag{1}$$

The resulting strain is a statistical ensemble of lattice strains from a subset of grains that satisfy the diffraction condition for the chosen crystallographic plane $\{hkl\}$.

The measurable lattice strain contains IG strains, which are caused by plastic incompatibility between neighboring grains. As discussed in (Gnäupel-Herold et al., 2012), the IG strains do not change in the event of unloading. However, the reference d_0-spacing at unloads is not directly measurable due to the presence of IG strain. In the current study, the reference d_0-spacing at unloads was calculated by averaging the measured *d*-spacings at all probed orientations. Therefore, the IG strain ε^{IG} was estimated through:

$$\varepsilon^{IG}(hkl, \phi, \psi) = \frac{d_u(hkl, \phi, \psi) - \langle d_u \rangle}{\langle d_u \rangle} \tag{2}$$

where $\langle d_u \rangle$ is the average of all available *d*-spacings at unloads. Note that the elastic lattice strain $\varepsilon^{el}(hkl, \phi, \psi)$, which is used for diffraction analysis, should exclude the influence of the IG strain as in below Eq. (3)

$$\varepsilon^{el}(hkl, \phi, \psi) = \varepsilon^{X}(hkl, \phi, \psi) - \varepsilon^{IG}(hkl, \phi, \psi), \tag{3}$$

in which ε^{X} is the experimentally measured in situ strains. The final lattice strain ε^{el} is linearly proportional to the applied macro stress, thus should follow a generalized formulation of Hooke's law:

$$\varepsilon^{el}(hkl, \phi, \psi) = F_{ij}(hkl, \phi, \psi)\langle \sigma_{ij} \rangle, \tag{4}$$

where $F_{ij}(hkl, \phi, \psi)$ denotes the diffraction elastic constants, i.e., the stress factors; $\langle \sigma_{ij} \rangle$ is the average stress over the whole volume, which is assumed to be equal to the macroscopic stress of the representative polycrystalline aggregate. In the case of constant ϕ and *hkl*, Eq. (4) simplifies to

$$\varepsilon^{el}(\psi) = F(\psi)\langle \boldsymbol{\sigma} \rangle. \tag{5}$$

In isotropic residual stress analysis, lattice strain $\varepsilon^{el}(\psi)$ are linearly proportional to $\sin^2\psi$ values. In the case of current anisotropic IF steel, Fig. 3 shows the experimentally measured lattice strains exhibit a curved slope when plotted against the $\sin^2\psi$ values. Therefore, stress analysis for the current IF steel sample requires an independent determination for the stress factors either by model or by experiment.

The IF steel sample was strained as described earlier in Section 2.2. The in situ X-ray measurement was performed at various punch positions (thus 20 different plastic strains) during the biaxial stretching up to effective strain of about 0.9.

Lattice *d*-spacings obtained at a prescribed plastic strain level can be expressed in terms of lattice strain using Eq. (1) with the reference d_0 as the average of all the measured *d*-spacings at the probed orientations.

To complete the stress analysis, lattice strains and stress factors are used to calculate the stress, using the procedures described in Gnäupel-Herold et al. (2014a). To estimate the stress factors, small dog-bone samples are cut from the biaxially deformed samples at the prescribed strains. The dog-bone samples are elastically loaded during which the changes in elastic strain $\varepsilon^{el}(hkl, \phi, \psi)$ are recorded at various macroscopic stress levels. Each stress factor component F_{ij} was obtained by linear regression of $\varepsilon^{el}(hkl, \phi, \psi)$ against the applied macroscopic stress. For example, uniaxial tensions along $\langle \sigma_{11} \rangle$ and $\langle \sigma_{22} \rangle$ allow measurements of F_{11} and F_{22}, that are corresponding to RD and TD, respectively.

Please cite this article in press as: Jeong, Y., et al. Evaluation of biaxial flow stress based on elasto-viscoplastic self-consistent analysis of X-ray diffraction measurements. Int. J. Plasticity (2014), http://dx.doi.org/10.1016/j.ijplas.2014.06.009

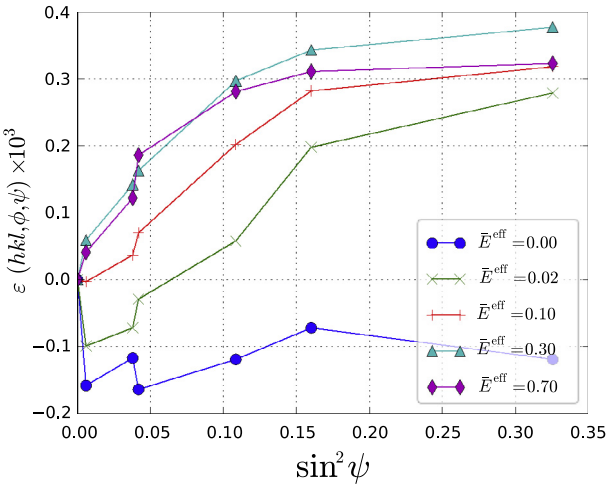

Fig. 3. Experimental lattice strains measured at selected increments of biaxial stretching in an IF steel sample. The displayed data were taken at the effective strain levels of 0.0, 0.02, 0.10, 0.30 and 0.70. The typical uncertainty in strain (1 × sigma) is ≈2 × 10^{-5}).

Nominally, stress factors at each plastic strain level should be separately determined. However, the experimental measurements of stress factors were limited to only 4 different plastic strain levels including the as-received status (i.e., $\bar{E}^{\text{eff}}$ = 0; 0.20; 0.50; 0.70), as a set of measurements for each stress factor component at a given plastic strain level requires a separate sample (Gnäupel-Herold et al., 2012; Ortner, 2006). Stress factors for intermediate plastic strain levels were interpolated from these data. It is noted that the prestrained samples were used to measure the IG strains at unloads as well.

After stress factors and IG strains were measured, the IG strains were subtracted using Eq. (3) to obtain the load proportional lattice strains $\varepsilon^{\text{el}}(hkl,\phi,\psi)$. Based on Eq. (4), provided that the stress factor $F_{ij}(hkl,\phi,\psi)$ is known, the macroscopic stresses $\langle\sigma_{ij}\rangle$ can be calculated through a numerical procedure such as the least-square method (Hauk, 1997).

4. Polycrystal model

Due to the burden required to characterize stress factors and IG strains experimentally, accurate models are desired. Various models have been developed in the literature spanning from classical 'bound' type models, such as Voigt (1910) and Reuss (1929), to some advanced models describing more realistic grain-interactions (Gnäupel-Herold et al., 2012). These grain-interaction models between a grain and the surrounding medium can be estimated following the Eshelby approach (Gnäupel-Herold et al., 2012; Kneer, 1965; Kröner, 1958).

The models mentioned above consider only the elastic constitutive behaviors, thus consideration of plastic influence due to changes in grain morphology and texture on the stress factor and IG strain requires additional input to account for changes in texture and grain morphology. Changes in texture can be obtained by experiments or by an independent model. The modeling procedure performed by in Gnäupel-Herold et al. (2014b) links two different modeling frameworks, (1) VPSC (Lebensohn and Tomé, 1993) for texture evolution and (2) elastic polycrystal models based on Eshelby to estimate stress factor and IG strain, which can make the stress analysis difficult for widespread use. Application of an elasto-viscoplastic crystal plasticity model (EVPSC) (Wang et al., 2010) may be more useful because it can concurrently perform both required modeling tasks – texture prediction and calculation of stress factor and IG strain. The suitability of the EVPSC model for stress analysis is claimed by the fact that all the aforementioned influencing factors are intrinsically embedded in this approach – such as texture evolution and interactions between grains and the surrounding matrix.

4.1. EVPSC scheme

For a grain, the viscoplastic constitutive description (relation between the viscoplastic local strain rate $\dot{\varepsilon}^{\text{vp}}$ and the local stress σ) is expressed as follows (Lebensohn and Tomé, 1993; Molinari et al., 1987):

$$\dot{\boldsymbol{\varepsilon}}^{\text{vp}} = \gamma_0 \sum_s \boldsymbol{m}^s \left(\frac{\boldsymbol{m}^s : \boldsymbol{\sigma}}{\tau_c^s} \right)^n \tag{6}$$

where the superscript s denotes a slip system; $\boldsymbol{m}^s$ and $\boldsymbol{\sigma}$ denote the Schmid tensor and the local stress tensor, respectively; γ_0 and τ_c^s are the normalization factors for the power law relation between the slip shear rate and the resolved shear stress; n is the exponent of the power law, which is set here as 20. The above Eq. (6) is linearized for further treatments as:

$$\dot{\boldsymbol{\varepsilon}}^{\text{vp}} = \mathbb{m}^{\text{vp}} : \boldsymbol{\sigma} + \dot{\boldsymbol{\varepsilon}}^{\text{vp}^0} \tag{7}$$

Please cite this article in press as: Jeong, Y., et al. Evaluation of biaxial flow stress based on elasto-viscoplastic self-consistent analysis of X-ray diffraction measurements. Int. J. Plasticity (2014), http://dx.doi.org/10.1016/j.ijplas.2014.06.009

where $\mathbb{m}^{vp}$ and $\dot{\boldsymbol{\varepsilon}}^{vp^0}$ are viscoplastic local moduli and the back-extrapolated term resulting from the linearization, respectively. Likewise, the macroscopic behavior assumes the same linear formulation:

$$\dot{\overline{\boldsymbol{E}}}^{vp} = \overline{\mathbb{M}}^{vp} : \overline{\Sigma} + \dot{\overline{\boldsymbol{E}}}^{vp^0} \tag{8}$$

where $\overline{\Sigma}$, $\dot{\overline{\boldsymbol{E}}}^{vp}$, $\overline{\mathbb{M}}^{vp}$ and $\dot{\overline{\boldsymbol{E}}}^{vp^0}$ are the macroscopic stress, viscoplastic strain rate, compliance and back-extrapolated strain rate, respectively.

The viscoplastic strain rate becomes a function of the macroscopic property by adapting Hutchinson's method (Hutchinson, 1976):

$$\dot{\varepsilon}^{vp} = \overline{\mathbb{M}}^{vp} : \boldsymbol{\sigma} + \dot{\overline{\boldsymbol{E}}}^{vp^0} + \dot{\varepsilon}^{vp^*} \tag{9}$$

in which $\dot{\boldsymbol{\varepsilon}}^{vp^*}$ is the eigenstrain (Lebensohn et al., 2007; Mura, 1987).

The Eshelby solution for a fully anisotropic viscoplastic medium is employed to calculate the local deviation ($\dot{\tilde{\boldsymbol{\varepsilon}}}^{vp}$) from the macroscopic strain:

$$\dot{\tilde{\boldsymbol{\varepsilon}}}^{vp} = \mathbb{S}^{vp} : \dot{\boldsymbol{\varepsilon}}^{vp^*} \tag{10}$$

where the $\mathbb{S}^{vp}$ denotes the corresponding Eshelby tensor. The procedure to calculate the viscoplastic Eshelby tensor is detailed in Lebensohn et al. (2007) and Tomé and Lebensohn (2009).

The elastic response is calculated based on the elastic inclusion problem. Assuming the additive decomposition, the total strain is equal to the sum of the viscoplastic and elastic contributions:

$$\dot{\varepsilon} = \overline{\mathbb{M}}^{e} : \dot{\boldsymbol{\sigma}} + \overline{\mathbb{M}}^{vp} : \boldsymbol{\sigma} + \hat{\dot{\varepsilon}}^{vp^0} \tag{11}$$

where $\overline{\mathbb{M}}^{e}$ and $\hat{\dot{\varepsilon}}^{vp^0}$ are the macroscopic instantaneous elastic compliance tensor and the viscoplastic back-extrapolated strain term. Additional details on the EVPSC model can be found in Wang et al. (2010).

4.2. EVPSC model parameters

In the EVPSC model, the single crystal elastic constants for iron (Rotter and Smith, 1966), listed in Table 1, were used.

Crystallographic texture measurements were made on bulk as received material at the NIST Center for Neutron Research. These data were used to generate a polycrystal population of 20,000 discrete grains for the EVPSC model. The initial grain morphology was assumed to be spherical for all grains.

4.3. Slip system and strain hardening

Slip was assumed to occur on two systems, i.e., $\{1\,1\,0\}\langle 1\,1\,1\rangle$ and $\{1\,1\,2\}\langle 1\,1\,1\rangle$. The hardening on individual slip system was expressed through an empirical hardening law (Tomé et al., 1984):

$$\tau_c^s = \tau_0^s + (\tau_1^s + \theta_1^s \Gamma)\left(1 - \exp\left(-\Gamma\left|\frac{\theta_0^s}{\tau_1^s}\right|\right)\right), \tag{12}$$

where τ_c^s is the critical resolved shear stress for the slip system s and Γ denotes the accumulated shear strain ($\Gamma = \sum_s \gamma^s$ with γ^s being the shear on each slip system s). It was also assumed that the slip systems undergo isotropic Taylor-type strain hardening, by which all slip systems harden in an equal rate regardless of their orientation. The four parameters τ_0^s, τ_1^s, θ_0^s and θ_1^s of Eq. (12) were determined by fitting with the experimental effective flow stress curve obtained by the bulge test. The hardening parameter optimization was iteratively carried out using the Simplex method developed in Nelder and Mead (1965) and extended for a polycrystal model in Jeong et al. (2012). The optimized hardening parameters are listed in Table 2.

4.4. X-ray emulation conditions

A subroutine that simulates the diffraction conditions of the current in situ X-ray diffraction system was implemented into the original EVPSC code. All the variants of the $\{2\,1\,1\}$ plane in a grain are examined to determine if they are oriented such that their normal n^{hkl} is within a particular angular distance ω^w with the bisecting normal n^d of the X-ray beam. During the present work, ω^w of 2° was used. Only those grains having a $\{2\,1\,1\}$ variant appropriately oriented for the prescribed orientations (ϕ, ψ) may contribute to $\varepsilon(211, \phi, \psi)$.

Table 1
Iron single crystal constants in (GPa) from Rotter and Smith (1966).

$\mathbb{C}_{11}$	$\mathbb{C}_{12}$	$\mathbb{C}_{44}$
231.4	134.7	116.4

Please cite this article in press as: Jeong, Y., et al. Evaluation of biaxial flow stress based on elasto-viscoplastic self-consistent analysis of X-ray diffraction measurements. Int. J. Plasticity (2014), http://dx.doi.org/10.1016/j.ijplas.2014.06.009

Table 2
Hardening parameters in (MPa).

τ_0	τ_1	θ_0	θ_1
79.3	73.7	340	19.9

4.5. Model calculation for stress factor and intergranular strain

The calculation for stress factor and IG strain using EVPSC was performed through a virtual experiment following the procedures described in Section 3. As illustrated in the flow chart given in Fig. 4 the model prediction for stress factor and IG strain are performed at specified intervals of simulated biaxial stretching. To simulate the experimental conditions, the polycrystal is fully unloaded when it reaches the prescribed plastic strain, after which the stress factor and the IG strain are calculated by applying uniaxial elastic loads to the simulated sample. In contrast to the real experiment, the model can additionally calculate the IG strain even when the sample is under load, provided that the stress factor is known. IG strain at load can be estimated using Eq. (13) obtained by combining Eqs. (3) and (4):

$$\varepsilon^{IG}(hkl,\phi,\psi) = \varepsilon^{M}(hkl,\phi,\psi) - F_{ij}(hkl,\phi,\psi)\overline{\Sigma}_{ij}. \tag{13}$$

where ε^{M} indicates the model-predicted diffraction strain that corresponds to the experimental counterpart ε^{X} in Eq. (3); $\overline{\Sigma}_{ij}$ denotes the macroscopic stress that is volume average stress of all constituent grains. Note that the individual stress factor component F_{ij} is obtained from the subsequent uniaxial reloading of the unloaded polycrystal to match the experimental method.

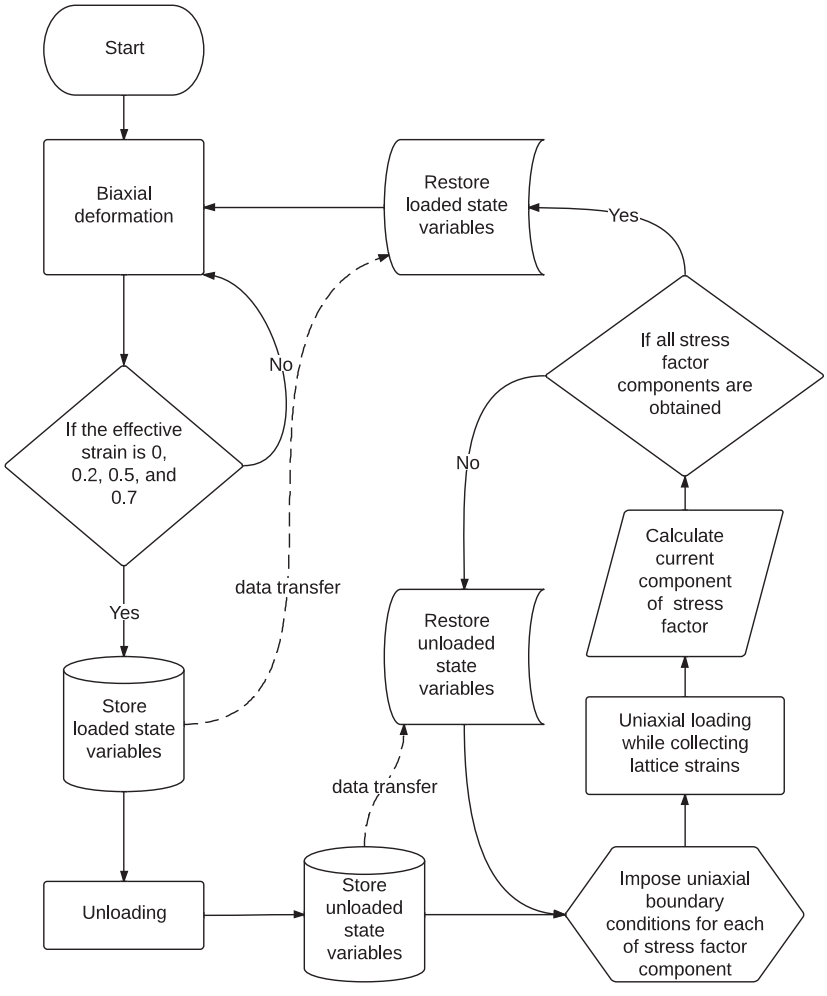

Fig. 4. Flow chart for stress factors calculation using the EVPSC model.

Please cite this article in press as: Jeong, Y., et al. Evaluation of biaxial flow stress based on elasto-viscoplastic self-consistent analysis of X-ray diffraction measurements. Int. J. Plasticity (2014), http://dx.doi.org/10.1016/j.ijplas.2014.06.009

5. Comparison between model predictions and experimental results

5.1. Texture development

Sections from the bulge sample were used to measure the texture developed by the biaxial stretching. The specimen for the texture measurement underwent a biaxial deformation of about 0.9 effective strain. Fig. 5 shows the pole figures of as-received sample (5a) and at 0.9 effective strains both by experiment (5b) and by model (5c). As shown in Fig. 5b and c the experimental and model-predicted pole figures are in an excellent agreement.

The {2 1 1} pole figure is of particular interest in that the same diffraction plane was exclusively used for the diffraction stress analysis. According to the model prediction in Fig. 6, it is shown that the volume distribution of grains in diffraction condition in the probed orientations significantly changes as texture develops. It is confirmed that grains are not completely

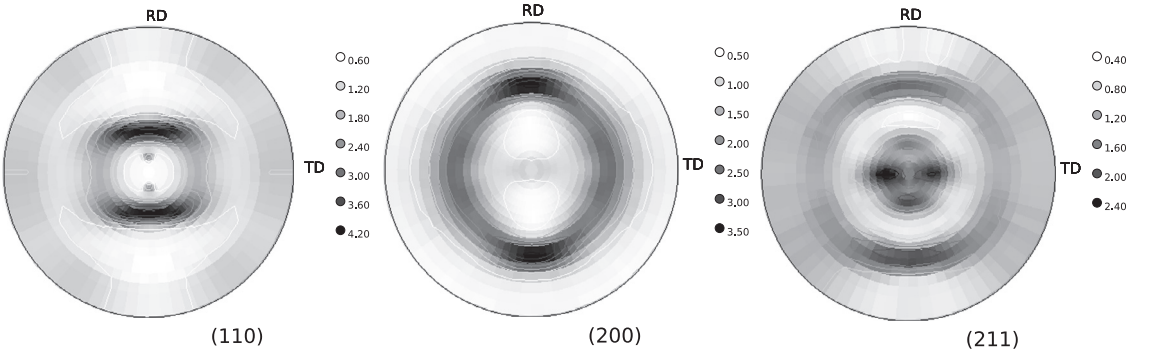

(a) Experimental pole figures for the as-received IF steel sample

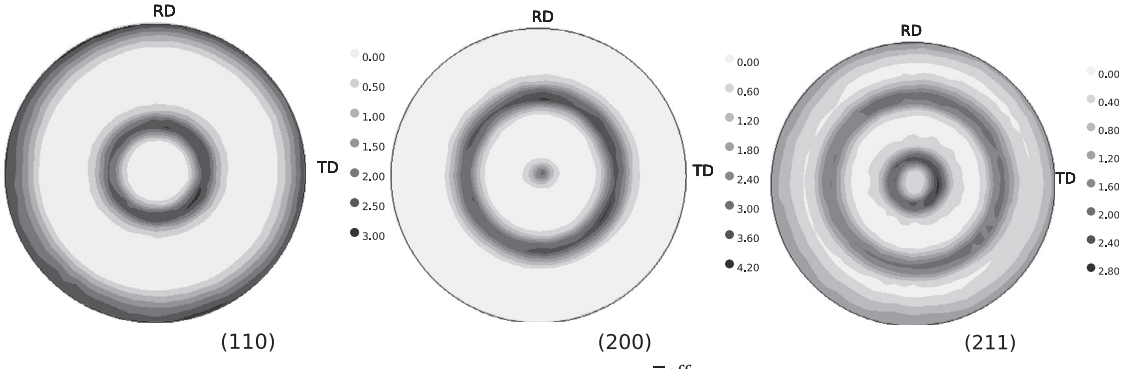

(b) Experimental pole figures at $\bar{E}^{\text{eff}} = 0.9$

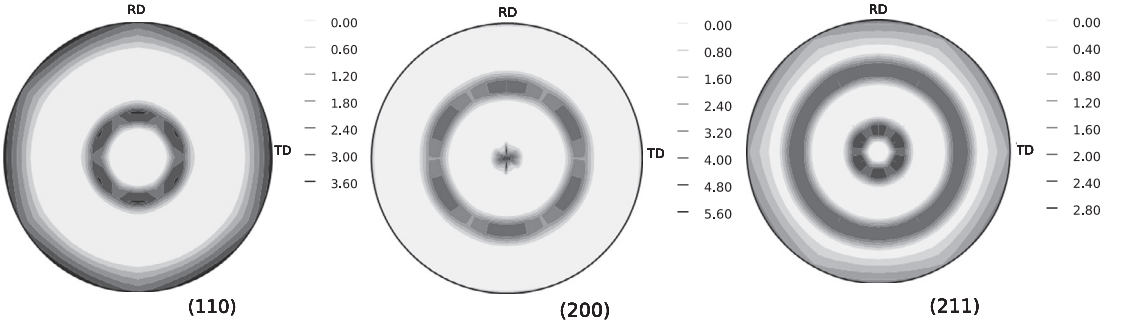

(c) EVPSC-predicted pole figures at $\bar{E}^{\text{eff}} = 0.9$

Fig. 5. Experimental and model-predicted pole figures.

Please cite this article in press as: Jeong, Y., et al. Evaluation of biaxial flow stress based on elasto-viscoplastic self-consistent analysis of X-ray diffraction measurements. Int. J. Plasticity (2014), http://dx.doi.org/10.1016/j.ijplas.2014.06.009

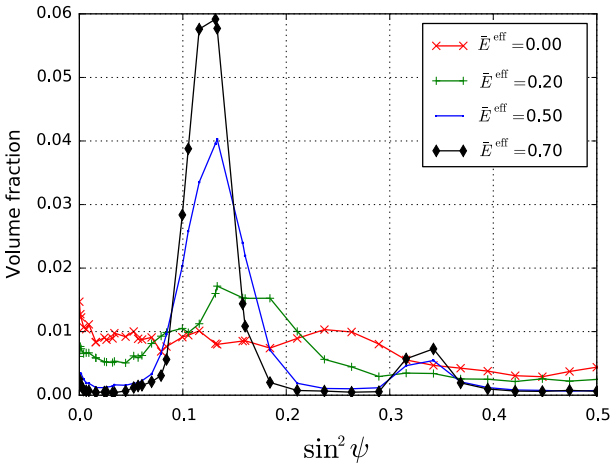

Fig. 6. Volume fractions of grains in diffraction condition for $(\phi = 0°, \psi)$ at various effective strains.

depleted in the probed range of ψ angles for {2 1 1} diffraction. At high deformations, however, the volume fraction of diffracting grains is lower than 0.1% of the total at certain ψ angles. A similar depletion of diffraction volume is inferred for the experimental sample based on the similarities of the {2 1 1} pole figures in Fig. 5b and c.

5.2. Uniaxial tension and bulge test

In Fig. 7 the computationally predicted uniaxial and bulge flow curves are compared with the experimental results. The uniaxial tension flow behavior seems isotropic comparing RD, TD and DD. The yield stress (at 0.2% macro strain) is approximately 150 MPa in both bulge test and uniaxial tension tests. However, the difference between the bulge and uniaxial tension in terms of the hardening rate is significant. For instance, the flow stress differential between bulge test and uniaxial tension reaches around 100 MPa at the effective strain of 0.3. This result demonstrates that there is a significant difference in hardening rate between the biaxial and uniaxial deformation modes, even in cases where the initial yield stress does not differ. Fig. 8 is a comparison between the *r*-values measured experimentally and predicted computationally. The EVPSC model tends to underestimate the *r*-values as depicted in Fig. 8. Nevertheless, in general, the model predictions are also in qualitatively good agreement with experimental results.

It is noted here that the simulation results, particularly the quantitative hardening differential between the uniaxial and biaxial (bulge) curves, were influenced by the choice of the linearization method in Eq. (6). – readers are directed to

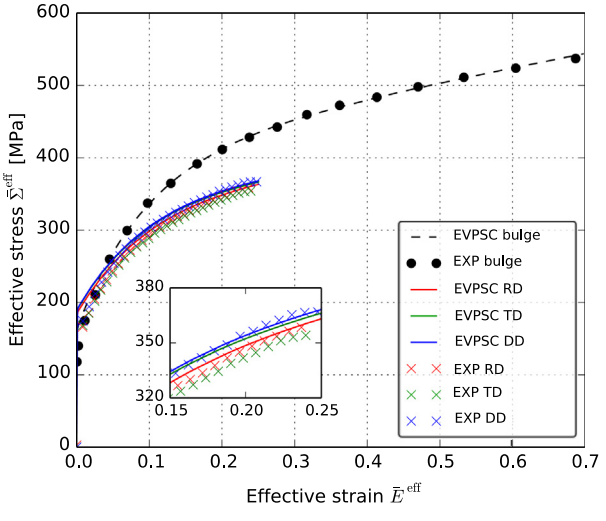

Fig. 7. Effective flow stress–strain curves of experimental bulge test and uniaxial tensions along RD, TD and DD together with their simulative counterparts by EVPSC.

Please cite this article in press as: Jeong, Y., et al. Evaluation of biaxial flow stress based on elasto-viscoplastic self-consistent analysis of X-ray diffraction measurements. Int. J. Plasticity (2014), http://dx.doi.org/10.1016/j.ijplas.2014.06.009

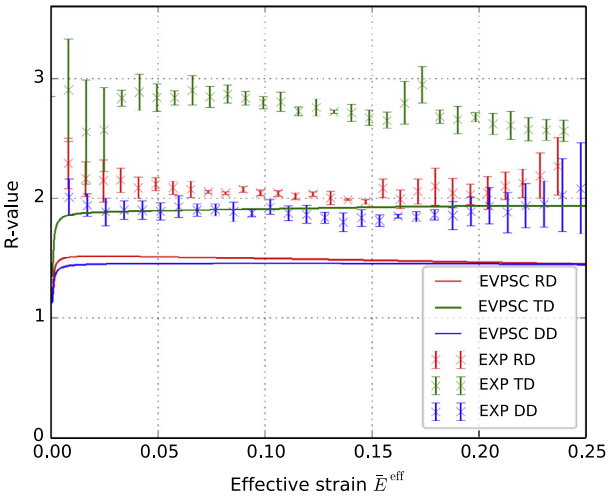

Fig. 8. Experimental and EVPSC-predicted *R*-values along RD, TD, and DD.

Lebensohn et al. (2007) for detailed information on the linearization methods. For the current IF steel sample, the tangent method gave the best agreement among other linearization schemes in terms of the hardening differential. Therefore, the simulation conducted in current study exclusively used the tangent method. It is, however, worth noting that any available linearization scheme resulted in a qualitatively consistent trend.

5.3. Stress factor comparison

Both experimental and model-predicted stress factors are presented in Fig. 9. The stress factors are plotted against $\sin^2\psi$ values at various biaxial strain levels. The F_{11} prediction (Fig. 9a) clearly shows a dip at $\sin^2\psi = 0.35$ after a strain of $\bar{E}^{\text{eff}} = 0.2$. However, in the experimental counterpart (Fig. 9b), this trend is not obvious except at $\bar{E}^{\text{eff}} = 0.5$. The predicted F_{22} curves are somewhat deviated from their experimental counterparts. The model prediction of F_{22} (Fig. 9a) shows a systematic and consistent downward shift as plastic deformation increases. However, the experimental results (Fig. 9b) exhibit neither the consistent downward shift nor any noticeable systematic trend. Nevertheless, deviation in F_{22} seems minor compared to that in F_{11}. Overall, model predictions on both components can be considered in reasonable agreement with the experiment. Although not shown here, model predictions along other ϕ angles ($-90°$ and $45°$) are in good agreement with experiment as well.

5.4. Intergranular strain comparison

The experimental IG strains are shown in Fig. 10. It is found that (a) IG strains, at all probed plastic levels, have a highest strain of about 100 micro strain ($\mu\varepsilon$) at the $\sin^2\psi = 0$ (along ND of the sample); (b) Also, IG strains tend to decrease as the diffraction normal is further tilted from the ND; (c) Furthermore, it seems that there is no systematic influence of plastic deformation on the IG strain evolution. These mentioned characteristics (a, b, and c) are commonly observed in other ϕ angles ($45°$, and $-90°$), which are not presented here.

Model-predicted IG strains calculated both at loads and unloads are given in Fig. 11. It is found that the influence of unloading on IG strain is negligible as assumed earlier in Section 3. However, the model-predicted IG strain differs from what is experimentally observed: the experimental IG strain has values in between $-60\mu\varepsilon$ and $120\mu\varepsilon$, whereas the model-predicted IG strains span from $-500\mu\varepsilon$ to $500\mu\varepsilon$ in the probed ψ angles. Also, it is found that the calculated IG strain has a systematic development with respect to the plastic deformation, which is conflicted with the experimental trend that plastic deformation does not show any noticeably systematic influence. Also, the model is not capable of predicting decreases of IG strain as the tilting angle ψ increases as $\sin^2\psi$ value increases from 0 to 0.2 as shown in Fig. 10. Instead, the predicted trend is quite the opposite that the model prediction shows an increasing trend in the mentioned $\sin^2\psi$ range.

In the literature, it has been reported that lattice strain, as the total $\varepsilon(hkl, \phi, \psi)$ that includes both ε^{el} and ε^{IG}, calculated by models similar to the current EVPSC exhibited a noticeable discrepancy with experimental result particularly along the direction perpendicular to loading (Clausen et al., 1999; Daymond et al., 2000; Kanjarla et al., 2012; Neil et al., 2010). Also, it is rare to find comparison of the computational prediction with experimentally measured IG strain explicitly, which is an important element in the current stress analysis. However, none of the mentioned studies discuss the accuracy of the IG strain prediction made by polycrystal models. The cause of the discrepancy between the predicted IG strain and the experimental result presented in this study is not clearly understood.

Please cite this article in press as: Jeong, Y., et al. Evaluation of biaxial flow stress based on elasto-viscoplastic self-consistent analysis of X-ray diffraction measurements. Int. J. Plasticity (2014), http://dx.doi.org/10.1016/j.ijplas.2014.06.009

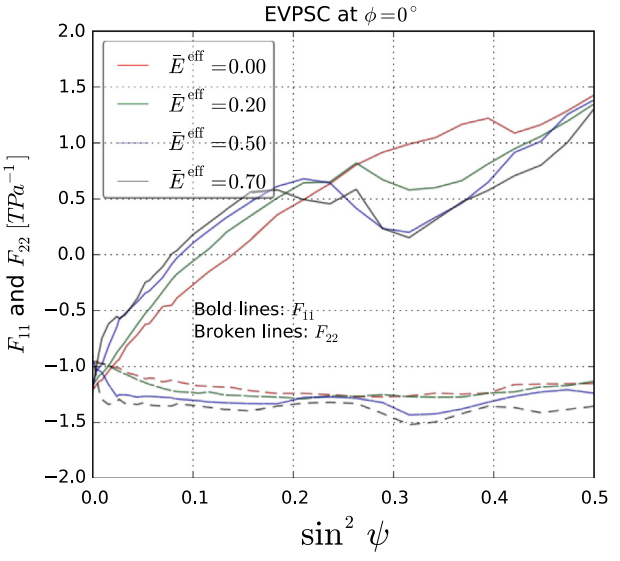

(a) EVPSC predicted F_{11} and F_{22} at $\phi = 0^\circ$

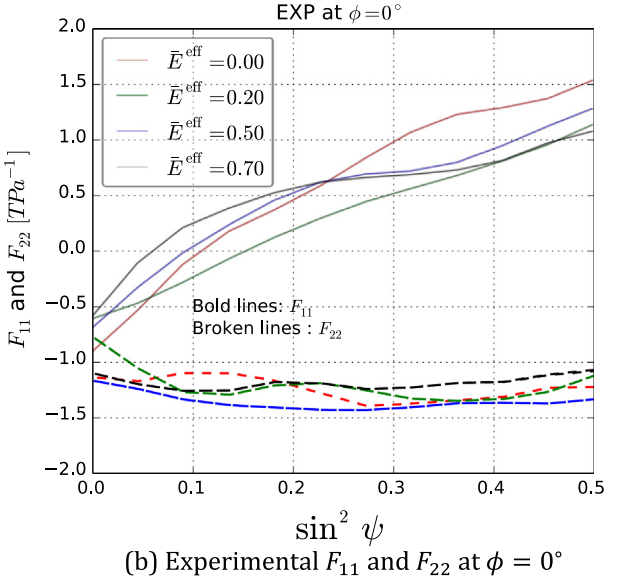

(b) Experimental F_{11} and F_{22} at $\phi = 0^\circ$

Fig. 9. Stress factor comparison in terms of two major components F_{11} and F_{22} at the effective strain levels shown in the legend: (a) model predictions and (b) experimental results. The orientations in the present results are (ϕ = 0°, ψ).

5.5. Results of stress analysis and comparison with bulge test

In the current section, the biaxial flow curves based on the X-ray stress analysis are presented in comparison with that of the bulge test. First of all, as demonstrated earlier, the use of proper stress factors for the current IF steel sample are required. As shown in Section 5.3, the model-predicted stress factor was in qualitatively good agreement with experiments. On the contrary, as discussed in Section 5.4, the model-predicted IG strain was not in good agreement with the experimental values. As a result, consideration of the model-predicted IG strain led to an unrealistic softening in flow behavior (Fig. 12). Meanwhile, relatively reasonable flow stress is obtained when excluding the ill-predicted IG strain from consideration. Therefore, in what follows, the model-predicted IG strain is not further considered in X-ray stress analysis.

In Fig. 13, biaxial flow stress curves based on stress analysis using the experimental IG strain (curves (a) and (b) as denoted in the legend) are displayed. Also, the flow curve based on the model stress factor without IG strain subtraction is also shown (curve (c)). In addition, the result of the bulge test (curve (d)) is included as a reference. Curve (a) shows that diffraction stress analysis using the experimental stress factor and IG strain results in good agreement with the bulge test

Please cite this article in press as: Jeong, Y., et al. Evaluation of biaxial flow stress based on elasto-viscoplastic self-consistent analysis of X-ray diffraction measurements. Int. J. Plasticity (2014), http://dx.doi.org/10.1016/j.ijplas.2014.06.009

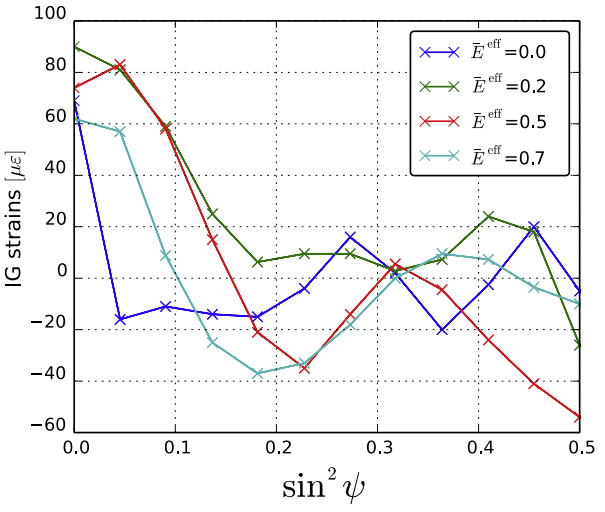

Fig. 10. IG strains measured on the samples that are fully unloaded using X-ray diffraction for ($\phi = 0°, \psi$). The uncertainties ($1 \times$ sigma) are approximately $15\mu\varepsilon$.

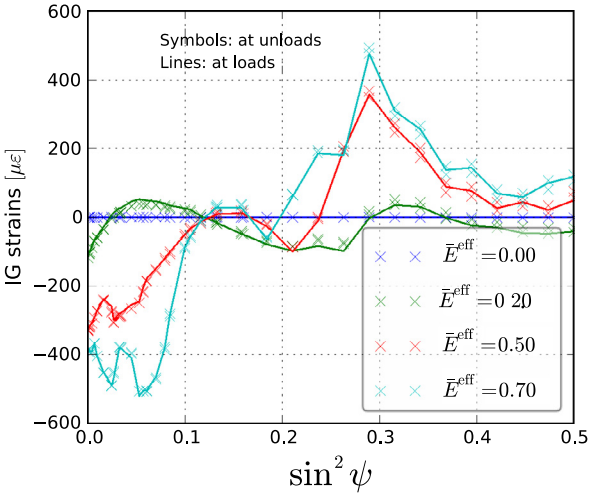

Fig. 11. Change of IG strains predicted by EVPSC at both unloads (symbols) and loads (lines) for ($\phi = 0°, \psi$). Each tilt angle ψ contains two points corresponding to the positive and negative tilt.

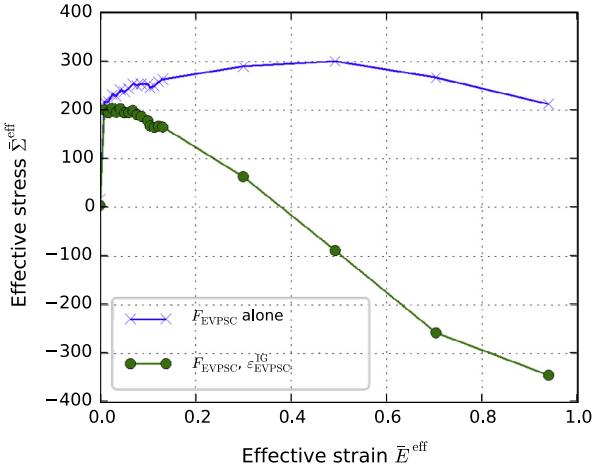

Fig. 12. The flow curves obtained through the stress analysis using the X-ray in situ *d*-spacings. The stress analysis was conducted based on the model-predicted stress factor (F_{EVPSC}): (1) with and (2) without subtraction of the model-predicted IG strain ($\varepsilon^{\text{IG}}_{\text{EVPSC}}$) (circles and crosses, respectively).

Please cite this article in press as: Jeong, Y., et al. Evaluation of biaxial flow stress based on elasto-viscoplastic self-consistent analysis of X-ray diffraction measurements. Int. J. Plasticity (2014), http://dx.doi.org/10.1016/j.ijplas.2014.06.009

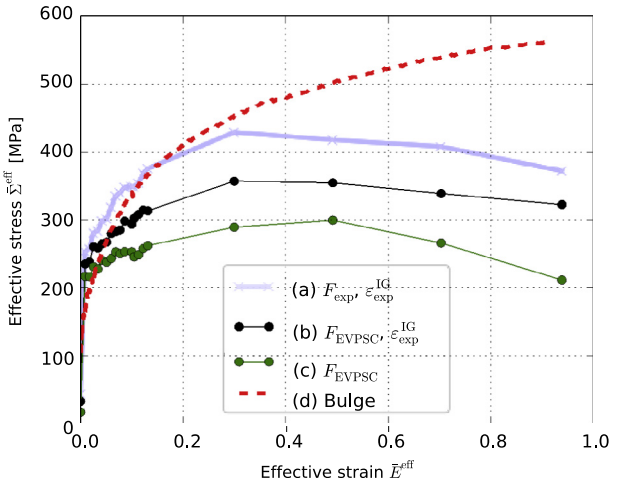

Fig. 13. Effective flow curves shown here are obtained from stress analysis using (a) experimental pair of stress factor and IG strain and (b) estimation made only by the model-predicted stress factor with experimental IG. Also flow curves (c) is the result of the model-predicted without any IG strain input strains. In addition, the reference flow curve obtained by the hydraulic bulge test (d) is included.

flow curve up to the effective strain of 0.5. Data points at the effective strains of 0.70 and 0.94 show unrealistic strain softening. The difference with the reference bulge curve is reduced by considering the experimental IG strains as depicted in the curves (b) and (c). The difference with the bulge curve further decreases by replacing the model stress factor with the experimental counterpart as depicted in curve (a).

Not shown are a series of uniaxial tests with displacement holds of a similar duration to the hold required for an in situ X-ray diffraction measurement. In these displacement hold tests, a stress drop of about 20 MPa was observed. The lower stresses observed when compared with the bulge test may be related to this relaxation.

6. Summary and discussions

In this study, the experimental biaxial flow curves were obtained by two biaxial tests: (1) Marciniak test with in situ X-ray diffraction and (2) hydraulic bulge test. The X-ray stress analysis for the Marciniak test accompanied the use of stress factor and IG strain measured on the separately prestrained samples. In addition, an elasto-viscoplastic self-consistent crystal plasticity model was used to calculate the stress factor and the IG strain.

The predictive capability of the EVPSC model was confirmed based on texture (Section 5.1) and hardening differential between uniaxial and biaxial deformation modes (Section 5.2). Also, the predicted stress factor components, both F_{11} and F_{22}, were in good qualitative agreement with their experimental counterparts (Section 5.3). However, the model prediction of the IG strain exhibited a noticeable discrepancy with the experiment (Section 5.4). As a consequence, it led to the unrealistic flow curves when used for the stress analysis (Section 5.5). By disregarding the erroneous model prediction for IG strain, an improvement was made. Yet, the results based on the combination of the model-predicted stress factor and experimental IG strain led to an unrealistic result. The stress analysis based on the pair of experimental stress factor and IG strain was relatively more successful in that the flow behavior up to the effective strain of 0.2 is in good agreement with the reference bulge curve. Yet, a significant amount of unrealistic strain softening was observed at large deformations. A part of this failure is due to the stress relaxation that occurs during the displacement holding for the in situ *d*-spacing measurements. Nevertheless, the resulting unrealistic softening at large deformation was a major drawback of the current stress analysis technique, which prevented any rigorous comparison with the hydraulic bulge test.

It was also found that the simulation results support the assumption that IG strain is insensitive to unloading. On the other hand, certain improvements for the model are required in that the IG strain prediction significantly differs from its experimental counterpart. The difference found between the predicted and experimental IG strains might be related with the prediction of poorer quality often reported in the literature along directions perpendicular to loading (Clausen et al., 1999, 1998; Daymond et al., 2000; Kanjarla et al., 2012) in steel samples based on similar models. More fundamentally, the IG strain represents the degree of inhomogeneity between grains. For example, it was reported that the 'multisite modeling' to account for more realistic interactions between grains improved predictive accuracy (Delannay et al., 2002). Therefore, the current failure of IG strain prediction suggests improvements in the current constitutive descriptions particularly regarding the inhomogeneous response of grains in response to the interaction with the surrounding matrix.

7. List of notations

Vectors and tensors are written in bold except when expressed with its indices, following the Einstein convention.

Please cite this article in press as: Jeong, Y., et al. Evaluation of biaxial flow stress based on elasto-viscoplastic self-consistent analysis of X-ray diffraction measurements. Int. J. Plasticity (2014), http://dx.doi.org/10.1016/j.ijplas.2014.06.009

- ϕ: Azimuthal angle from rolling direction of sheet (for details see Section 2.2).
- ψ: Tilt angle from sheet normal (for details see Section 2.2).
- (ϕ, ψ): An orientation pertaining to a certain volume of material in diffraction.
- hkl: Miller indices of planes in diffraction condition.
- ε^{el}: Elastic strain.
- ε^{X}: Experimentally measurable elastic strain by diffraction.
- ε^{IG}: Intergranular (IG) strain.
- d: Interplanar lattice d-spacing.
- d_0: d-spacing in the absence of external stress.
- $\boldsymbol{F}$: Stress factor.
- $\boldsymbol{\sigma}$: Local stress.
- $\overline{\boldsymbol{\Sigma}}$: Macroscopic stress.
- $\overline{\boldsymbol{E}}$: Macroscopic strain.

Acknowledgements

Youngung Jeong acknowledges that a part of this work was conducted during his stay at Los Alamos National Laboratory (LANL) hosted by Dr. Carlos Tomé. This work was supported by POSCO and by the National Research Foundation of Korea (NRF) Grant funded by the Korea government (MSIP) (No. 2012R1A5A1048294). Dr. Huamiao Wang in LANL kindly provided the original code of the EVPSC model. The X-ray diffraction experiments with Marciniak tooling was due to Youngung Jeong's stay in National Institute of Standards and Technology (NIST), which was sponsored by Dr. Timothy Foecke. Assistance performing the Marciniak test by Mr. David Pitchure and Hyukjong Bong are kindly acknowledged. Also, assistance on the bulge test analysis by Dr. Jin Kim and Ms. Jeong Yeon Lee are kindly acknowledged.

References

Barlat, F., Maeda, Y., Chung, K., Yanagawa, M., Brem, J.C., Hayashida, Y., Lege, D.J., Matsui, K., Murtha, S.J., Hattori, S., Becker, R.C., Makosey, S., 1997. Yield function development for aluminum alloy sheets. J. Mech. Phys. Solids 45, 1727–1763.
Barlat, F., Brem, J.C., Yoon, J.W., Chung, K., Dick, R.E., Lege, D.J., Pourboghrat, F., Choi, S.-H., Chu, E., 2003. Plane stress yield function for aluminum alloy sheets-part 1: theory. Int. J. Plast. 19, 1297–1319.
Barlat, F., Aretz, H., Yoon, J.W., Karabin, M.E., Brem, J.C., Dick, R.E., 2005. Linear transformation-based anisotropic yield functions. Int. J. Plast. 21, 1009–1039.
Barral, M., Lebrun, J.L., Sprauel, J.M., Maeder, G., 1987. X-ray macrostress determination on textured material; use of the ODF for calculating the X-ray compliances. Metall. Mater. Trans. A 18, 1229–1238.
Bong, H.J., Barlat, F., Lee, M.-G., Ahn, D.C., 2012. The forming limit diagram of ferritic stainless steel sheets: experiments and modeling. Int. J. Mech. Sci.
Clausen, B., Lorentzen, T., Leffers, T., 1998. Self-consistent modelling of the plastic deformation of f.c.c. polycrystals and its implications for diffraction measurements of internal stresses. Acta Mater. 46, 3087–3098.
Clausen, B., Lorentzen, T., Bourke, M.A.M., Daymond, M.R., 1999. Lattice strain evolution during uniaxial tensile loading of stainless steel. Mater. Sci. Eng., A 259, 17–24.
Daymond, M.R., Tomé, C.N., Bourke, M.A.M., 2000. Measured and predicted intergranular strains in textured austenitic steel. Acta Mater. 48, 553–564.
Delannay, L., Logé, R.E., Chastel, Y., Van Houtte, P., 2002. Prediction of intergranular strains in cubic metals using a multisite elastic-plastic model. Acta Mater. 50, 5127–5138.
Foecke, T., Iadicola, M.A., Lin, A., Banovic, S.W., 2007. A method for direct measurement of multiaxial stress-strain curves in sheet metal. Metall. Mater. Trans. A 38A, 306–313.
Gnäupel-Herold, T., Creuziger, A.A., Iadicola, M., 2012. A model for calculating diffraction elastic constants. J. Appl. Crystallogr. 45, 197–206.
Gnäupel-Herold, T., Iadicola, M.A., Creuziger, A.A., Foecke, T., Hu, L., 2014a. Interpretation of diffraction data from in situ stress measurements during biaxial sheet metal forming. Mater. Sci. Forum Trans. Tech. Publ., 441–448.
Gnäupel-Herold, T., Gree, D.E., Foecke, T., Iadicola, M.A., 2014b. Through-thickness stresses in automotive sheet metal after plane strain channel draw. Mater. Sci. Forum 768, 433–440.
Hauk, V., 1997. Structural and Residual Stress Analysis by Nondestructive Methods: Evaluation–Application-Assessment. Elsevier Science.
Hill, R., 1948. A theory of the yielding and plastic flow of anisotropic metals. In: Proceedings of the Royal Society of London, Series A, Mathematical and Physical Sciences, vol. 193, pp. 281–297.
Hill, R., 1950. A theory of the plastic bulging of a metal diaphragm by lateral pressure. Phil. Mag. 41, 1133–1142.
Hill, R., 1979. Theoretical plasticity of textured aggregates. Math. Proc. Cambridge Philos. Soc. 85, 179–191.
Hutchinson, J.W., 1976. Bounds and self-consistent estimates for creep of polycrystalline materials. Proc. R. Soc. A 348, 101–127.
Iadicola, M.A., Gnäupel-Herold, T.H., 2012. Effective X-ray elastic constant measurement for in situ stress measurement of biaxially strained AA5754-O. Mater. Sci. Eng., A 545, 168–175.
Iadicola, M.A., Foecke, T., Banovic, S.W., 2008. Experimental observations of evolving yield loci in biaxially strained AA5754-O. Int. J. Plast. 24, 2084–2101.
Jeong, Y., Barlat, F., Lee, M.-G., 2012. Application of crystal plasticity to an austenitic stainless steel. Modell. Simul. Mater. Sci. Eng. 20, 024009.
Kanjarla, A.K., Lebensohn, R.A., Balogh, L., Tomé, C.N., 2012. Study of internal lattice strain distributions in stainless steel using a full-field elasto-viscoplastic formulation based on fast Fourier transforms. Acta Mater. 60, 3094–3106.
Kneer, G., 1965. Über die Berechnung der Elastizitätsmoduln vielkristalliner Aggregate mit Textur. Physica status solidi (b) 9, 825–838.
Kröner, E., 1958. Berechnung der elastischen Konstanten des Vielkristalls aus den Konstanten des Einkristalls. Zeitschrift für Physik A Hadrons and Nuclei 151, 504–518.
Kuwabara, T., 2007. Advances in experiments on metal sheets and tubes in support of constitutive modeling and forming simulations. Int. J. Plast. 23, 385–419.
Kuwabara, T., Ikeda, S., Kuroda, K., 1998. Measurement and analysis of differential work hardening in cold-rolled steel sheet under biaxial tension. J. Mater. Process. Technol. 80–81, 517–523.
Kuwabara, T., Yoshida, K., Narihara, K., Takahashi, S., 2005. Anisotropic plastic deformation of extruded aluminum alloy tube under axial forces and internal pressure. Int. J. Plast. 21, 101–117.
Lebedev, A.A., Muzyka, N.R., 1998. Design of cruciform specimens for fracture toughness tests in biaxial tension (review). Strength Mater 30, 243–254.

Please cite this article in press as: Jeong, Y., et al. Evaluation of biaxial flow stress based on elasto-viscoplastic self-consistent analysis of X-ray diffraction measurements. Int. J. Plasticity (2014), http://dx.doi.org/10.1016/j.ijplas.2014.06.009

Lebensohn, R.A., Tomé, C.N., 1993. A self-consistent anisotropic approach for the simulation of plastic deformation and texture development of polycrystals: application to zirconium alloys. Acta Metall. Mater. 41, 2611–2624.
Lebensohn, R.A., Turner, P.A., Signorelli, J.W., Canova, G.R., Tomé, C.N., 1998. Calculation of intergranular stresses based on a large-strain viscoplastic self-consistent polycrystal model. Modell. Simul. Mater. Sci. Eng. 6, 447.
Lebensohn, R.A., Tomé, C.N., Castñeda, P.P., 2007. Self-consistent modelling of the mechanical behaviour of viscoplastic polycrystals incorporating intragranular field fluctuations. Phil. Mag. 87, 4287–4322.
Lee, Y.-W., Woertz, J.C., Wierzbicki, T., 2004. Fracture prediction of thin plates under hemi-spherical punch with calibration and experimental verification. Int. J. Mech. Sci. 46, 751–781.
Logan, R.W., Hosford, W.F., 1980. Upper-bound anisotropic yield locus calculations assuming ⟨111⟩-pencil glide. Int. J. Mech. Sci. 22–6, 419–430.
Marciniak, Z., Kuczyński, K., Pokora, T., 1973. Influence of the plastic properties of a material on the forming limit diagram for sheet metal in tension. Int. J. Mech. Sci. 15, 789–800.
Mohr, D., Jacquemin, J., 2008. Large deformation of anisotropic austenitic stainless steel sheets at room temperature: multi-axial experiments and phenomenological modeling. J. Mech. Phys. Solids 56, 2935–2956.
Mohr, D., Oswald, M., 2008. A new experimental technique for the multi-axial testing of advanced high strength steel sheets. Exp. Mech. 48, 65–77.
Molinari, A., Canova, G.R., Ahzi, S., 1987. A self consistent approach of the large deformation polycrystal viscoplasticity. Acta Metall. 35, 2983–2994.
Mura, T., 1987. Micromechanics of Defects in Solids. Springer.
Neil, C.J., Wollmershauser, J.A., Clausen, B., Tomé, C.N., Agnew, S.R., 2010. Modeling lattice strain evolution at finite strains and experimental verification for copper and stainless steel using in situ neutron diffraction. Int. J. Plast. 26, 1772–1791.
Nelder, J.A., Mead, R., 1965. A simplex method for function minimization. Comp. J. 7, 308–313.
Noyan, I.C., Cohen, J.B., 1986. Residual stress.
Ortner, B., 2006. Symmetry properties and transformation behavior of the X-ray stress factors. J. Appl. Crystallogr. 39, 401–409.
Ranta-Eskola, A.J., 1979. Use of the hydraulic bulge test in biaxial tensile testing. Int. J. Mech. Sci. 21, 457–465.
Reuss, A., 1929. Berechnung der Fließgrenze von Mischkristallen auf Grund der Plastizitätsbedingung für Einkristalle. ZAMM – Journal of Applied Mathematics and Mechanics/Zeitschrift für Angewandte Mathematik und Mechanik 9, 49–58.
Rotter, C.A., Smith, C.S., 1966. Ultrasonic equation of state of iron: I. Low pressure, room temperature. J. Phys. Chem. Solids 27, 267–276.
Stoughton, T.B., 2000. A general forming limit criterion for sheet metal forming. Int. J. Mech. Sci. 42, 1–27.
Stoughton, T.B., Zhu, X., 2004. Review of theoretical models of the strain-based FLD and their relevance to the stress-based FLD. Int. J. Plast. 20, 1463–1486.
Tasan, C.C., Hoefnagels, J.P.M., Dekkers, E.C.A., Geers, M.G.D., 2012. Multi-axial deformation setup for microscopic testing of sheet metal to fracture. Exp. Mech. 52, 669–678.
Tomé, C.N., Lebensohn, R.A., 2009. Manual for code Visco-Plastic Self-Consistent (VPSC).
Tomé, C., Canova, G.R., Kocks, U.F., Christodoulou, N., Jonas, J.J., 1984. The relation between macroscopic and microscopic strain hardening in F.C.C. polycrystals. Acta Metall. 32, 1637–1653.
Turner, P.A., Tomé, C.N., 1994. A study of residual stresses in Zircaloy-2 with rod texture. Acta Metall. Mater. 42, 4143–4153.
Verma, R.K., Murakoso, S., Chung, K., Kuwabara, T., 2010. Material Modeling and springback prediction of ultra thin austenitic stainless steel sheet. In: The 10th International conference on Numerical Methods in Industrial Forming Processes.
Voigt, W., 1910. Lehrbuch der kristallphysik. BG Teubner.
Wang, H., Wu, P.D., Tomé, C.N., Huang, Y., 2010. A finite strain elastic–viscoplastic self-consistent model for polycrystalline materials. J. Mech. Phys. Solids 58, 594–612.
Wong, S.L., Dawson, P.R., 2010. Influence of directional strength-to-stiffness on the elastic–plastic transition of fcc polycrystals under uniaxial tensile loading. Acta Mater. 58, 1658–1678.
Wu, P.D., Graf, A., MacEwen, S.R., Lloyd, D.J., Jain, M., Neale, K.W., 2005. On forming limit stress diagram analysis. Int. J. Solids Struct. 42, 2225–2241.
Xu, L., Barlat, F., 2008. Disk compression testing and constitutive modeling of TWIP sheet sample. Proc. ICTP 2008, 2312–2317.

Please cite this article in press as: Jeong, Y., et al. Evaluation of biaxial flow stress based on elasto-viscoplastic self-consistent analysis of X-ray diffraction measurements. Int. J. Plasticity (2014), http://dx.doi.org/10.1016/j.ijplas.2014.06.009